A Coil Positioning Method Integrated With an Orthogonal Decoupled Transformer for Inductive Power Transfer Systems

Zhuhaobo Zhang, *Student Member, IEEE*, Shaoting Zheng, *Student Member, IEEE*,
Zirui Yao, *Student Member, IEEE*, Dehong Xu, *Fellow, IEEE*, Philip T. Krein, *Life Fellow, IEEE*,
and Hao Ma, *Senior Member, IEEE*

***Abstract*—Misalignment between primary and secondary coils in inductive power transfer systems decreases power capacity and efficiency. In this article, a secondary coil positioning method integrated with an orthogonal decoupled transformer is proposed. This nested rectangular and solenoidal structure consists of a pair of double-D coils and a pair of solenoidal coils. The coils are integrated spatially and decoupled magnetically. Based on their directional selectivity characteristics, a coil positioning method is proposed prior to the power path activation. Coordinates can be obtained with polynomial fit calculations. The positioning method is compatible with power transfer and has merits of less auxiliary equipment, higher compatibility, and higher positioning precision considering both horizontal and vertical misalignment cases. The transformer performance is simulated with a three-dimensional finite element modeling tool and verified experimentally on a 3.2-kW prototype. In the preactivation sensing process, points distributed throughout a ±180 mm × 180 mm positioning range were tested. Experimental results show that 92% of tested points are accurate to within 10 mm given a 210 mm vertical distance. When air gap variations are taken into consideration, 90% of tested points are accurate to within 12 mm over the tested range. In the power transfer stage, the maximum full-power dc–dc system efficiency is 94.6%.**

***Index Terms*—Coil positioning, inductive power transfer (IPT), misalignment, orthogonal decoupled transformer, wireless power.**

I. INTRODUCTION

INDUCTIVE power transfer (IPT) technology is attractive for electric vehicle (EV) charging and to increase EV range [1]–[3]. Limitations because of low primary–secondary coupling, misalignment, and unwanted stray coupling are issues. In this article, a receiver coil positioning method, integrated with an orthogonal decoupled transformer, is proposed to address these issues and improve on recent designs. The proposed configuration enhances directional selectivity such that coil position can be calculated and adjusted.

Loosely coupled transformers are important in IPT systems. Unipolar and bipolar structures have been considered [4]–[6]. Circular and rectangular coils represent unipolar structures. Their magnetic fluxes are symmetrical in horizontal directions. Bipolar structures, such as solenoidal and double-D (DD) coils, have a dominant magnetic flux direction along their cores.

Compared to a single pair of coils, transformers with multiple transmitters and multiple receivers have been explored for lower cost, higher power transfer capability, and better system compatibility in [7]–[14]. Decoupled transformer structures are preferred because cross-coupling will affect power flow and resonant frequencies [7]. Two decoupled solenoidal coils were used with an orthogonal arrangement in [8] and a diagonal arrangement in [9]. One obvious drawback of these designs is that space was not used effectively. A few integrated designs have been proposed. A DDQ structure was proposed in [5] and a double-sided decoupled transformer was presented in [10]. To enhance the misalignment range, a quadrature pick-up was proposed in [11] with two decoupled solenoidal coils, and a DD2Q receiver was presented in [12] with two bipolar coils. A similar target was achieved in [13] and [14] with two pairs of orthogonal triangular coils and cross-shaped hybrid DD coils. The integration of multiple orthogonal decoupled coils helps to increase available output power.

For IPT transformers, misalignment between transmitter and receiver coils decreases power capacity and efficiency. Much research has been conducted to improve misalignment performance from coil structure [5], [6], compensation network [15], [16], and circuit topology [17], [18] aspects. In practice, misalignment tolerance mitigation is limited. To confirm that the receiver is within the charging area, a position detection method

Manuscript received July 6, 2021; revised November 2, 2021 and January 11, 2022; accepted February 18, 2022. Date of publication March 1, 2022; date of current version April 28, 2022. This work was supported in part by the National Natural Science Foundation of China under Grant 51977190, and in part by the Zhejiang University/University of Illinois at Urbana-Champaign Institute. Recommended for publication by Associate Editor D. Zhang. *(Corresponding author: Hao Ma.)*

Zhuhaobo Zhang, Zirui Yao, and Hao Ma are with the College of Electrical Engineering, Zhejiang University, Hangzhou 310027, China, and also with the Zhejiang University/University of Illinois at Urbana-Champaign Institute, Haining 314400, China (e-mail: zzhbpain@163.com; 11810009@zju.edu.cn; mahao@zju.edu.cn).

Shaoting Zheng and Dehong Xu are with the College of Electrical Engineering, Zhejiang University, Hangzhou 310027, China (e-mail: 3150103536@zju.edu.cn; dehongxu@yahoo.com).

Philip T. Krein is with the College of Electrical Engineering, Zhejiang University, Hangzhou 310027, China, with the Zhejiang University/University of Illinois at Urbana-Champaign Institute, Haining 314400, China, and also with the University of Illinois at Urbana-Champaign, Champaign, IL 61820 USA (e-mail: krein@illinois.edu).

Color versions of one or more figures in this article are available at https://doi.org/10.1109/TPEL.2022.3155270.

Digital Object Identifier 10.1109/TPEL.2022.3155270

is indispensable, as described in standard J2954 [19]. Position detection can be combined with autonomous parking technology to align the power coils. Costs for misalignment mitigation and positioning accuracy are compromise choices.

Existing coil positioning methods for IPT employ sensors or infer location from signal and power transmission behavior. Radio frequency (RF) readers and tags were employed in [20]. Cameras or infrared devices support optical methods [21]. Magnetoresistance (MR) and Hall sensor arrays have been investigated [22]–[24]. So far, RF and optical positioning have had limited application to EV charging because integration complexity is high and the sensors are relatively expensive. In [24], sensor count was reduced to drop costs, and sensor arrangements and ferrite core effects were discussed.

For positioning based on signal and power transmission, auxiliary coils on the secondary side can be used. Magnetic fields generated by primary coils induce auxiliary coil voltages. The methods have advantages of low system cost, high positioning accuracy, and low integration complexity. In [25] and [26], four symmetrical auxiliary coils were employed, with tests of various coil placements and positioning algorithms. A set of nonoverlapping coils for IPT chargers was presented in [27]. Simultaneous metal object and vehicle position detection were achieved. In [28], three coils were mounted on the primary side with respective LC tanks. Impedance characteristics were used to measure relative coil position.

In this article, a secondary coil positioning method, integrated with an orthogonal decoupled transformer, is proposed. The nested rectangular and solenoidal (NRS) structure consists of a pair of DD coils and a pair of solenoidal coils. Dominant magnetic fluxes are along respective x- and y-axis directions. The coils are integrated spatially and decoupled magnetically. The configuration provides directional selectivity for coil misalignment. The secondary coil position coordinates can be calculated with fitting functions. This method can be extended to consider air gap variations. For one pair of coupling coefficients, a string of points can be obtained and each point is a potential position for one air gap distance. These coordinates can be distinguished by means of an auxiliary square coil. In practice, the proposed positioning method is applied before power transfer. Based on results, excessive misalignment can be compensated manually by a driver (assisted by in-vehicle displays or feedback) or automatically by control systems. The power transfer stage is activated during vehicle parking, only across a defined narrow misalignment range. Compared to prior methods, the proposed method has advantages of high misalignment ranges, high compatibility, and high positioning accuracy. It is compatible with power transfer and convenient to implement. Only one auxiliary square coil on the secondary side is needed for current measurements. No extra sources are required. High positioning accuracy can be achieved even with air gap variations.

The rest of this article is organized as follows. The NRS structure is presented in Section II. Circuit modeling and analysis are given in Section III. The proposed coil positioning method is shown in Section IV. Determination of intersection points, quadrants, and air gap distances is elaborated. In Section V, experimental results for coil positioning and power transfer are obtained from a 3.2-kW prototype. Finally, Section VI concludes this article.

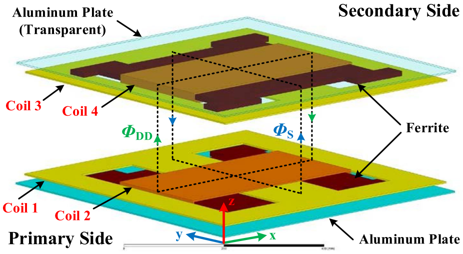

Fig. 1. Structure of the proposed orthogonal decoupled transformer.

II. TRANSFORMER STRUCTURE AND PERFORMANCE

A. Orthogonal Decoupled Transformer Structure

The proposed orthogonal decoupled transformer structure is shown in Fig. 1 [29]. Coil windings, ferrite cores, and aluminum plates are the three main components. Each part is marked with different colors and labeled. The secondary backside aluminum plate is shown as transparent. The primary and secondary sides are symmetrical about the z-axis.

The proposed NRS coil structure is used on both primary and secondary sides. There are two bipolar primary coils: DD coil 1 and solenoidal coil 2. Secondary coils 3 and 4 have the same arrangements. DD coils (coil 1 and coil 3) compose one energy transmission path and solenoidal coils (coil 2 and coil 4) compose another. As shown in Fig. 1, the magnetic flux generated by coil 1 is denoted as Φ_{DD} and is along the x-axis. This is the dominant flux coupling the DD coils. The flux generated by coil 2 is denoted as Φ_{S} and is along the y-axis. This is the dominant flux coupling the solenoidal coils. Φ_{DD} and Φ_{S} are orthogonal and decoupled when fully aligned. This also holds for x- and y-axis misalignment. The two power paths are integrated spatially and decoupled magnetically. This enhances system power transfer and reduces control complexity. DD coils and solenoidal coils are placed perpendicularly at overlap points to reduce proximity effects [30].

Ferrite cores are widely used in IPT systems for their high permeability. They reduce reluctance and enhance coupling. As distinct from conventional discrete placement of ferrite bars in DD or solenoidal couplers [4]–[6], the orthogonal structure requires low reluctance paths in both x and y axes. As shown in Fig. 1, ferrite cores are spaced tightly in the central region to minimize extraneous air gaps, with the coils arranged along the surface. Square aluminum plates behind the solenoidal coils help shield the backside magnetic flux. This reduces leakage fields and improves power coupling.

B. Finite Element Simulation and Analysis

IPT transformer pads seek to maximize quality factor Q and coupling coefficient k while minimizing weight and volume. Based on the proposed NRS structure, a top view and dimensions of the proposed pad structure are shown in Fig. 2(a). These are constrained by available space in a hypothetical EV. Values are listed in Table I. The overall dimensions of the primary and

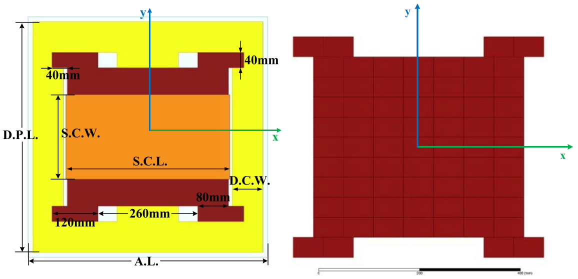

(a) (b)

Fig. 2. (a) Top view of pad structures with dimensions. (b) Top view of ferrite block arrangements.

TABLE I
SPECIFICATIONS OF THE PAD DIMENSIONS

Parameters	Symbols	Values
Ferrite blocks	/	60×40×10 [mm]
Ferrite thickness	**F.T.**	10 [mm]
Aluminum length	**A.L.**	625 [mm]
Aluminum thickness	**A.T.**	3 [mm]
DD pad length	**D.P.L**	600 [mm]
DD coil width	**D.C.W.**	80 [mm]
Solenoidal coil length	**S.C.L.**	480 [mm]
Solenoidal coil width	**S.C.W.**	220 [mm]
Transformer air gap distance	/	210 [mm]

secondary pads are 600 mm in length and 600 mm in width. The air gap is 210 mm in accordance with the Z3 class in standard J2954 [19]. A top view of the ferrite block arrangement is shown in Fig. 2(b). Each ferrite block is 60 mm × 40 mm × 10 mm. The dimensions, including the widths of DD coils (D.C.W.) and solenoidal coils (S.C.W.), have been optimized with a 3D finite element modeling (FEM) tool. Parametric simulation methods were employed to reach two targets: First, the two energy transmission paths should have identical maximum coupling coefficients when fully aligned. Solenoidal coils generally have higher coupling coefficients than DD coils due to the double-sided structure [5], [6]. As shown in Fig. 2(a) and (b), vacant sections on four sides compensate for coupling differences. Second, the DD and solenoidal coils should have approximately identical self-inductances for a given coil turns count. With these two targets, the two energy transmission paths can be treated symmetrically in circuit analysis. The maximum voltage gain and transferred power for each path are identical with *LCC* series compensation shown in Section III. The VA capacities of switching devices, passive components, and magnetic coils for each path are identical. This simplifies parameter design and component selection.

To demonstrate the coupling performance, simulation results of coupling coefficients versus various misalignment cases were explored, and results are shown in Fig. 3. A misalignment area of ± 200 mm × ± 200 mm was considered to provide an adequate margin for vehicle parking without auxiliary guidance devices. Parameter k_{13} is defined as the coupling coefficient between coils 1 and 3. Similar notation applies to coupling coefficients k_{24}, k_{14}, and k_{23}. Coefficients k_{13} and k_{24} represent power paths, whereas k_{14} and k_{23} are cross-couplings.

Variations of k_{13} and k_{24} with misalignment are shown in Fig. 3(a) and (b), respectively. The coefficients are nearly equal when there is no misalignment. They decrease as misalignment increases and behave differently in *x*- and *y*-axis directions for both DD and solenoidal coils. Because of the orthogonal structure, DD coils (k_{13}) behave better for *x*-axis misalignment and solenoidal coils (k_{24}) have more impact for *y*-axis misalignment. The misalignment characteristics are symmetric. This directional selectivity is an advantage of the NRS transformer structure and can be employed for the proposed coil positioning method. Corresponding implementation procedures are presented in Section IV.

Variations of k_{14} and k_{23} are shown in Fig. 3(c) and (d). Due to the orthogonal structure, these coefficients are very small for the fully aligned case and for misalignment cases in *x* and *y* directions. There is no directional selectivity for cross-coupling. In leading diagonal quadrants, cross-coupling coefficients are negative. Their absolute values increase gradually as misalignment increases. They are both positive in minor diagonal quadrants, with symmetrical misalignment in leading diagonal quadrants.

Solenoidal coils in Fig. 1 produce a two-sided flux path and only the flux path Φ_S is useful for power transfer [5], [6]. Magnetic flux density distribution simulated in the *yz*-plane with an FEM tool is shown in Fig. 4. The flux is excited with 6 A in both primary and secondary coils, based on 18 turns. The 27-μT contour, with the exposure limit value from [19], is marked with dotted lines. This shows good shielding effects on the backside of solenoidal coils.

III. CIRCUIT TOPOLOGY AND MODELING

As shown in Fig. 5(a), a circuit topology with *LCC* series compensation and an input-parallel output-series (IPOS) structure has been selected to drive the NRS transformer. Mutual inductance models the loosely coupled transformer, as represented by the shaded area. The primary circuit consists of two full-bridge inverters in parallel and two transmitter coils with *LCC* compensation. Each inverter is composed of four power MOSFETs (S_1–S_4). The secondary circuit consists of two full-bridge rectifiers (diodes D_1–D_4) in series and two receiver coils with single capacitor compensation. Inductances Lp1 (coil 1), Ls1 (coil 3) and Lp2 (coil 2), Ls2 (coil 4) correspond to self-inductances. Cross-coupling on the primary and secondary sides is close to zero and is not shown.

The fundamental harmonic approximation method [31] is used to analyze circuit characteristics. The equivalent mutual inductance circuit model is shown in Fig. 5(b). Ignoring high-order harmonics, define

$$\begin{cases} V_{\mathrm{p1}} = V_{\mathrm{p2}} = \frac{4}{\pi} V_{in} \\ V_{\mathrm{s1}} = \frac{4}{\pi} V_{\mathrm{o1}}, V_{\mathrm{s2}} = \frac{4}{\pi} V_{\mathrm{o2}} \\ R_{\mathrm{ac1}} = \frac{8R_{\mathrm{L}}}{\pi^2}\frac{V_{\mathrm{o1}}}{V_{\mathrm{o}}}, R_{\mathrm{ac2}} = \frac{8R_{\mathrm{L}}}{\pi^2}\frac{V_{\mathrm{o2}}}{V_{\mathrm{o}}} \end{cases} \tag{1}$$

where V_{in} and V_{o} are the system input and output dc voltages. V_{p1}, V_{p2} and V_{s1}, V_{s2} are the magnitudes of the fundamental harmonic voltages after the two inverters and before the two rectifiers. R_{L} and R_{ac1} and R_{ac2} are the load and system equivalent loads seen after and before each diode rectifier, respectively.

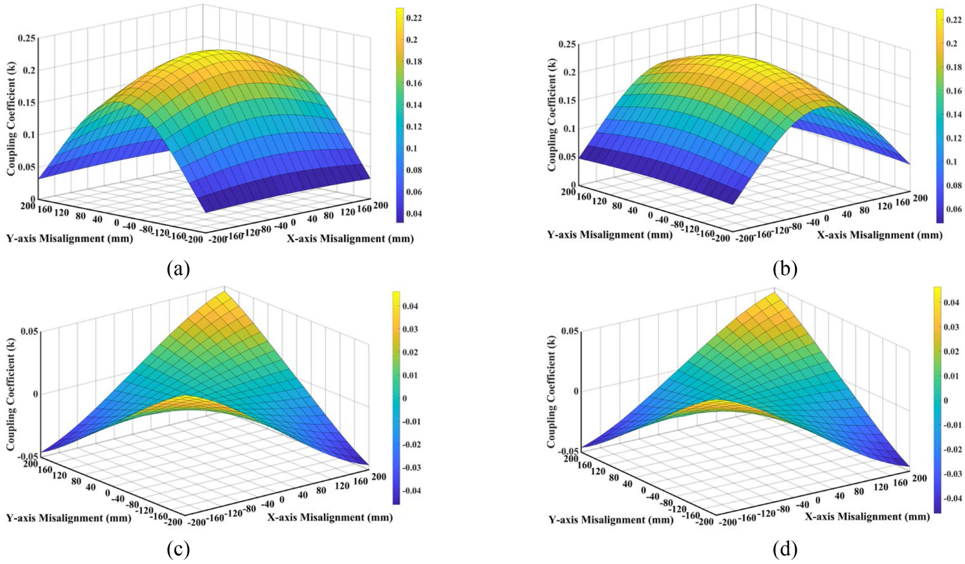

(a) (b) (c) (d)

Fig. 3. Coupling coefficients of (a) k_{13}, (b) k_{24}, (c) k_{14}, and (d) k_{23} for various misalignment cases.

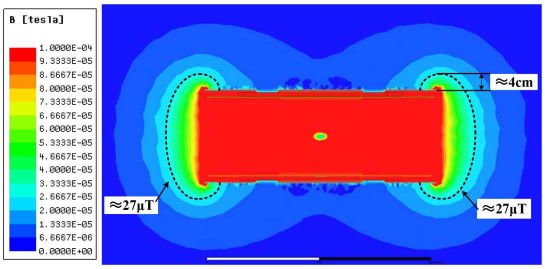

Fig. 4. Magnetic flux density distribution of the proposed NRS transformer in the *yz*-plane.

Impedance characteristics can be obtained from loop equations. The corresponding resonant condition is given by [32]

$$\omega = 2\pi f_{\mathrm{s}} = \frac{1}{\sqrt{L_{\mathrm{p3}}C_{\mathrm{p3}}}} = \frac{1}{\sqrt{L_{\mathrm{p4}}C_{\mathrm{p4}}}} = \frac{1}{\sqrt{L_{\mathrm{s1}}C_{\mathrm{s1}}}} = \frac{1}{\sqrt{L_{\mathrm{s2}}C_{\mathrm{s2}}}} = \sqrt{\frac{1}{L_{\mathrm{p1}}}\left(\frac{1}{C_{\mathrm{p1}}}+\frac{1}{C_{\mathrm{p3}}}\right)} = \sqrt{\frac{1}{L_{\mathrm{p2}}}\left(\frac{1}{C_{\mathrm{p2}}}+\frac{1}{C_{\mathrm{p4}}}\right)} \qquad (2)$$

where ω represents the system frequency in rad/s. In accordance with standard J2954 [19], the proposed system operating frequency is 85 kHz, but this can be adjusted slightly to optimize resonance. For the resonant condition, primary and secondary currents can be derived and are given by [33]

$$\dot{I}_{\mathrm{p1}} = \frac{\dot{V}_{\mathrm{p1}}}{j\omega L_{p3}}, \dot{I}_{\mathrm{p2}} = \frac{\dot{V}_{\mathrm{p2}}}{j\omega L_{p4}} \qquad (3)$$

$$\begin{cases} \dot{I}_{\mathrm{s1}} = \frac{j\omega M_{13}}{R_{\mathrm{ac1}}}\dot{I}_{\mathrm{p1}} + \frac{j\omega M_{23}}{R_{\mathrm{ac1}}}\dot{I}_{\mathrm{p2}} = \frac{\dot{V}_{\mathrm{p1}}}{R_{\mathrm{ac1}}}\frac{M_{13}}{L_{p3}} + \frac{\dot{V}_{\mathrm{p2}}}{R_{\mathrm{ac1}}}\frac{M_{23}}{L_{p4}} \\ \dot{I}_{\mathrm{s2}} = \frac{j\omega M_{24}}{R_{\mathrm{ac2}}}\dot{I}_{\mathrm{p2}} + \frac{j\omega M_{14}}{R_{\mathrm{ac2}}}\dot{I}_{\mathrm{p1}} = \frac{\dot{V}_{\mathrm{p2}}}{R_{\mathrm{ac2}}}\frac{M_{24}}{L_{p4}} + \frac{\dot{V}_{\mathrm{p1}}}{R_{\mathrm{ac2}}}\frac{M_{14}}{L_{p3}} \end{cases} \qquad (4)$$

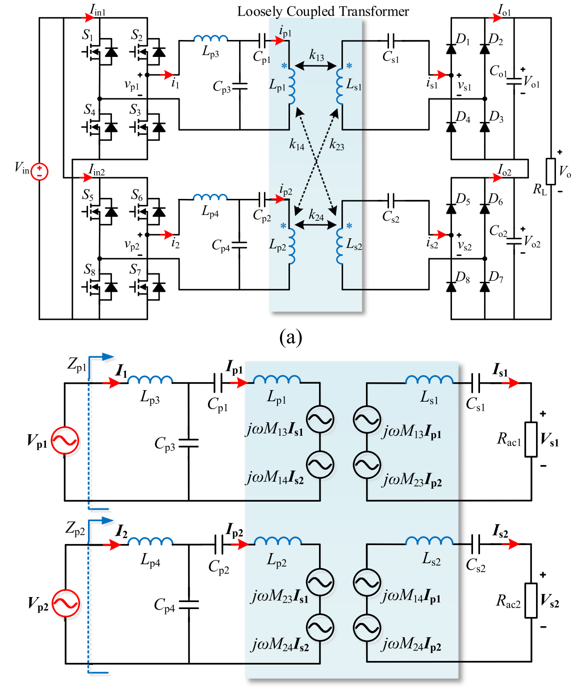

(b)

Fig. 5. (a) Circuit topology with *LCC* series compensation and an IPOS structure. (b) Equivalent mutual inductance circuit model.

$$\begin{cases} \dot{I}_1 = \dot{V}_{\mathrm{p1}}\left(\frac{{M_{13}}^2}{R_{\mathrm{ac1}}{L_{p3}}^2} + \frac{{M_{14}}^2}{R_{\mathrm{ac2}}{L_{p3}}^2}\right) \\ \quad + \dot{V}_{\mathrm{p2}}\left(\frac{M_{13}M_{23}}{R_{\mathrm{ac1}}L_{p3}L_{p4}} + \frac{M_{14}M_{24}}{R_{\mathrm{ac2}}L_{p3}L_{p4}}\right) \\ \dot{I}_2 = \dot{V}_{\mathrm{p1}}\left(\frac{M_{13}M_{23}}{R_{\mathrm{ac1}}L_{p3}L_{p4}} + \frac{M_{14}M_{24}}{R_{\mathrm{ac2}}L_{p3}L_{p4}}\right) \\ \quad + \dot{V}_{\mathrm{p2}}\left(\frac{{M_{23}}^2}{R_{\mathrm{ac1}}{L_{p4}}^2} + \frac{{M_{24}}^2}{R_{\mathrm{ac2}}{L_{p4}}^2}\right). \end{cases} \qquad (5)$$

From the specifications in Section II, the primary and secondary coil self-inductances are designed to match. Notation

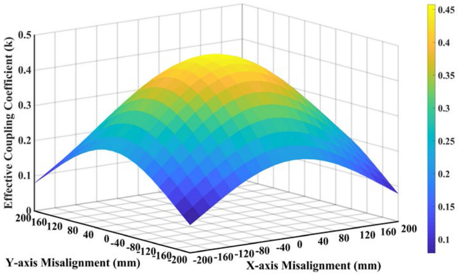

Fig. 6. Effective coupling coefficients of k_{eff} for various misalignment cases.

can be simplified as

$$\begin{cases} L_{p1} = L_{p2} = L_{\text{s1}} = L_{\text{s2}} = L_{\text{TR}} \\ L_{p3} = L_{p4} = L_{\text{C}}. \end{cases} \tag{6}$$

When the two primary inverters are controlled synchronously, the output dc voltage becomes

$$\begin{aligned} V_{\text{o}} &= \frac{\pi}{4}(|V_{\text{s1}}| + |V_{\text{s2}}|) \\ &= \frac{\pi}{4}\left(|\frac{M_{13}}{L_{p3}}V_{\text{p1}} + \frac{M_{23}}{L_{p4}}V_{\text{p2}}| + |\frac{M_{24}}{L_{p4}}V_{\text{p2}} + \frac{M_{14}}{L_{p3}}V_{\text{p1}}|\right) \\ &= \frac{V_{\text{in}}L_{\text{TR}}}{L_{\text{C}}}(|k_{13} + k_{23}| + |k_{24} + k_{14}|) \end{aligned} \tag{7}$$

where V_{p1} is equal to V_{p2}. This implies that the IPT system acts as a constant voltage source. The output voltage is independent of load resistance variation in the lossless case. An effective coupling coefficient of the overall transformer can be defined as

$$k_{\text{eff}} = |k_{13} + k_{23}| + |k_{24} + k_{14}|. \tag{8}$$

In practice, excessive misalignment can be compensated manually by a driver (assisted by in-vehicle displays or feedback) or automatically by control systems. Consequently, a narrow misalignment range, here ± 60 mm in both *x*- and *y*-axis directions, is considered for IPT charging. From Fig. 3(c) and (d), absolute values of coefficients k_{14} and k_{23} are below 0.01 and have little influence on circuit performance. Then, (7) and (8) can be simplified, and

$$V_{\text{o}} = \frac{V_{\text{in}}L_{\text{TR}}}{L_{\text{C}}}(k_{13} + k_{24}) = V_{\text{in}}\frac{M_{13} + M_{24}}{L_{\text{C}}} \tag{9}$$

$$k_{\text{eff}} = k_{13} + k_{24}. \tag{10}$$

The dc output power ratio $P_{\text{out1}}/P_{\text{out2}}$ is

$$\frac{P_{\text{out1}}}{P_{\text{out2}}} = \frac{V_{\text{o1}}I_{\text{o1}}}{V_{\text{o2}}I_{\text{o2}}} = \frac{V_{\text{o1}}}{V_{\text{o2}}} = \frac{k_{13}}{k_{24}}. \tag{11}$$

Equivalent misalignment characteristics are shown in Fig. 6 and behave similarly in *x*- and *y*-axis directions. From (9) to (11) and Fig. 6, the system power transfer capability is proportional to the sum of k_{13} and k_{24}.

TABLE II
SPECIFICATIONS OF PROTOTYPE IPT SYSTEM

Parameters	**Symbols**	**Values**
Nominal power rating	P_{o}	3.2 kW
Input voltage	V_{in}	300 V
Output voltage	V_{o}	400 V
Nominal load resistance	R_{L}	50 Ω

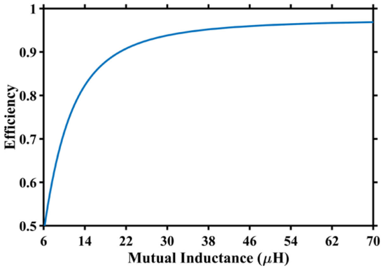

Fig. 7. System efficiency as a function of mutual inductance for the nominal 50 Ω load resistance.

Equivalent input impedances of the two primary inverters, i.e., Z_{p1} and Z_{p2}, are given by

$$Z_{p1} = \frac{\dot{V}_{\text{p1}}}{\dot{I}_1} = \left(\frac{L_C}{M_{12}}\right)^2 R_{\text{ac1}}, Z_{p2} = \frac{\dot{V}_{\text{p2}}}{\dot{I}_2} = \left(\frac{L_C}{M_{34}}\right)^2 R_{\text{ac2}}. \tag{12}$$

They are purely resistive, implying unity power factor. Reactive power in the resonant tanks is minimized. This benefits system efficiency.

Resonant circuit parameters can be selected based on the circuit modeling and system specifications in Table II. There, system power and voltage ratings have been selected based on an actual prototype for EV charging applications. The circuits in Fig. 5 can be separated into two independent ones. Parasitic resistances of transmitter coils and receiver coils are included as R_{p} and R_{s}. System efficiency for the k_{13} power path can be derived as [10]

$$\begin{aligned} \eta &= \frac{P_{\text{out1}}}{P_{\text{in1}}} = \frac{\text{Re}[\dot{V}_{\text{s1}}\,(\dot{I}_{\text{s1}})^*]}{\text{Re}[\dot{V}_{\text{p1}}\,(\dot{I}_1)^*]} \\ &= \frac{(\omega M_{13})^2 R_{ac1}}{(\omega M_{13})^2(R_{ac1} + R_{\text{s}}) + R_{\text{p}}(R_{ac1} + R_{\text{s}})^2}. \end{aligned} \tag{13}$$

The optimal load matching resistance $R_{\text{L(opt)}}$ to maximize efficiency η can be obtained by setting the derivative of η with respect to load to zero. This yields

$$R_{L(\text{opt})} = \frac{\pi^2}{4}\sqrt{\frac{(\omega M_{13})^2 R_{\text{s}} + R_{\text{p}}{R_{\text{s}}}^2}{R_{\text{p}}}} \tag{14}$$

where $R_{\text{L(opt)}}$ is approximately proportional to mutual inductance M_{13}. Equations (13) and (14) are employed to optimize system efficiency and to determine resonant parameter values. For nominal 50 Ω load resistance, the system efficiency as a function of mutual inductance is shown in Fig. 7. Parasitic resistances R_{p} and R_{s} are set to the estimated value of 0.4 Ω to model losses.

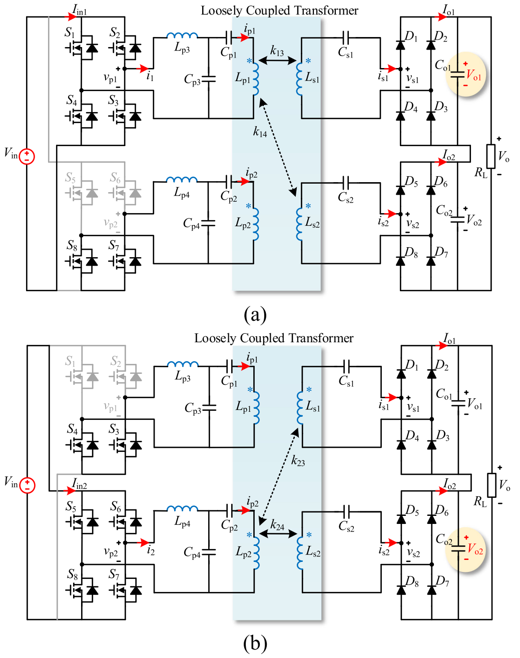

(a)

(b)

Fig. 8. Equivalent circuit topologies for coupling coefficients (a) k_{13} and (b) k_{24} calculations.

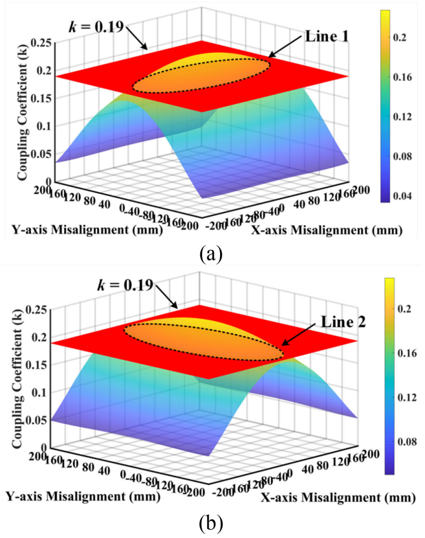

(a)

(b)

Fig. 9. Coupling coefficients of (a) k_{13} and (b) k_{24} for various misalignment cases with a fixed coupling coefficient of 0.19 and a 210 mm air gap distance.

In practice, the mutual inductance value of M_{13} is a compromise between efficiency improvement and the number of coil turns. This analysis can be extended to the k_{24} power path. The system efficiency reaches a maximum at nominal output power. Based on the mutual inductance selection in Fig. 7, the value of L_c can be obtained from (9). For the nominal coupling coefficient from Fig. 3, transmitter and receiver coil self-inductance L_{TR} can be determined. Resonant capacitor parameters can be calculated from (2). It is worth emphasizing that the circuit shown in Fig. 5 acts as a constant voltage source. In practice, a subsequent dc–dc converter can be employed to achieve impedance matching with the EV battery.

IV. COIL POSITIONING METHOD

Based on the circuit modeling and analysis in Section III, system power enhancement can be achieved with the proposed NRS transformer and IPOS circuit structure. In practice, power transfer should be activated only when the vehicle location falls within the defined narrow misalignment range. Before power transfer is enabled, a separate preactivation sensing process is needed to determine the coil position. Based on the directional selectivity of the NRS transformer, a coil position sensing method is proposed in this section.

A. Intersection Point Determination

Before charging, the two power transmission paths are used to calculate coupling coefficients k_{13} and k_{24} based on circuit voltage gains. As shown in Fig. 8(a), to accomplish this, the inverter in the k_{13} path is activated with 50% duty ratio or a predetermined phase-shifted angle α. This provides a method to limit transferred energy during the preactivation sensing process. The output dc voltage V_{o1} is measured. Switches S_7 and S_8 are turned ON to ensure parallel resonance of L_{p4} and C_{p4}. The resonant current i_{p2} is nearly zero. In this case, V_{o1} is linked only to k_{13} due to the orthogonal decoupled structure. Consequently, k_{13} can be calculated as

$$k_{13} = \frac{V_{o1} + 2V_F}{V_{in} - 2I_{in1}R_{ds(ON)}} \frac{1}{\cos(\alpha/2)} \frac{L_C}{L_{TR}} \left(1 + \frac{R_s}{R_{ac1}}\right) \quad (15)$$

where V_F and $R_{ds(ON)}$ are the forward diode voltage drop and the MOSFET ON-state resistance. Typically, parasitic resistance R_s is small compared to load resistance, so k_{13} can be estimated as

$$k_{13} \approx \frac{V_{o1} + 2V_F}{V_{in} - 2I_{in1}R_{ds(ON)}} \frac{1}{\cos(\alpha/2)} \frac{L_C}{L_{TR}}. \quad (16)$$

Coefficient k_{24} can be found similarly. As shown in Fig. 8(b), switches S_3 and S_4 are turned ON to ensure parallel resonance of L_{p3} and C_{p3}. The output dc voltage V_{o2} is measured with the inverter active in the k_{24} path, and

$$k_{24} \approx \frac{V_{o2} + 2V_F}{V_{in} - 2I_{in2}R_{ds(ON)}} \frac{1}{\cos(\alpha/2)} \frac{L_C}{L_{TR}}. \quad (17)$$

Based on values from (16) and (17) and misalignment characteristics in Fig. 3, two intersection lines and four intersection points can be determined. Fig. 9(a) and (b) shows the intersection of two surfaces as dotted lines. One surface represents coupling coefficient variations from Fig. 3(a) and (b). The other surface shows calculated values of k_{13} and k_{24} from (16) and (17). In Fig. 9, the values are both set to 0.19.

The dotted lines in Fig. 9 are replotted in Fig. 10. From Fig. 3, misalignment characteristics of the NRS transformer structure are symmetrical with respect to the x and y axes. This results in symmetry of lines 1 and 2. Intersection points A–D represent four symmetrical positions, distributed across four quadrants. Each point meets the coupling constraints of (16) and (17).

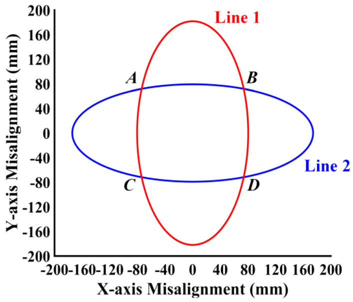

Fig. 10. Intersection lines 1 and 2 in one two-dimensional plane.

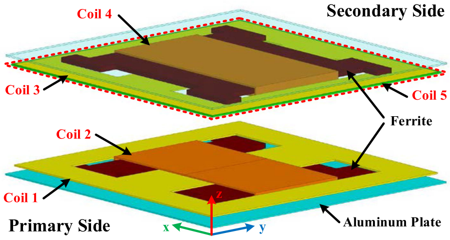

Fig. 11. Structure of the proposed orthogonal decoupled transformer with coil 5.

To obtain continuous relationships for coordinates of points *A*–*D*, a polynomial fit can be prepared. A quadratic fit gives

$$k(x,y) = p_{00} + p_{10}x + p_{01}y + p_{20}x^2 + p_{11}xy + p_{02}y^2 + p_{30}x^3 + p_{21}x^2y + p_{12}xy^2 + p_{03}y^3 \quad (18)$$

where p_{00}–p_{04} are obtained from least-squares analysis. From Fig. 9, fits are required for coupling coefficients k_{13} and k_{24}. Based on the results, coordinates of points *A*–*D* can be calculated. The efficacy of quadratic fits will be explored in the discussion of experimental results.

In practice, there may be a nonzero impedance angle for the load in IPT systems. In this case, the proposed positioning method is still effective due to the constant voltage source characteristics. Measurements of dc voltages V_{o1} and V_{o2} are not affected. This also holds for measurements of resonant currents i_{s1} and i_{s2} in a steady state.

B. Quadrant Determination

Points *A*–*D* are ambiguous with respect to the position because of symmetry. To determine the physical position, an auxiliary square coil 5 is added to the secondary side, as shown in Fig. 11. Coil 5 is distinct from the *Q* coil in the DDQ structure [5]. It is used for current measurements rather than for coupling enhancement, and is decoupled from the other coils when fully aligned. When misalignment occurs, coil 5 is still decoupled from coils 3 and 4 because their relative position is fixed. The coupling coefficient k_{15} is positive on the right side of *y*-axis and negative on the left side. Similarly, coefficient k_{25} is positive above the *x*-axis and negative below it. This directional selectivity supports quadrant determination to disambiguate points *A*–*D*.

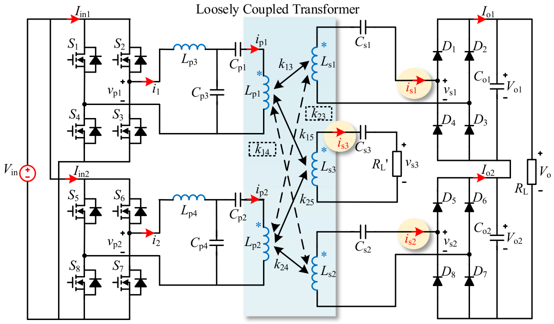

Fig. 12. Equivalent circuit topology with a secondary coil 5.

In Fig. 12, inductance L_{s3} (of the added third secondary) corresponds to the self-inductance of coil 5. In accordance with (2), capacitor C_{s3} resonates with L_{s3} at a fixed operating frequency of 85 kHz. $R_L{}'$ is an additional load resistance. For the resonant condition, current i_{s3} is given by

$$\dot{I}_{s3} = \frac{j\omega M_{15}}{R_L{}'}\dot{I}_{p1} + \frac{j\omega M_{25}}{R_L{}'}\dot{I}_{p2} = \frac{\dot{V}_{p1}}{R_L{}'}\frac{M_{15}}{L_{p3}} + \frac{\dot{V}_{p2}}{R_L{}'}\frac{M_{25}}{L_{p4}}. \quad (19)$$

Before power activation, phase relationships between currents i_{s1} and i_{s3} or i_{s2} and i_{s3} can be measured when respective inverters operate at a 50% duty ratio or a predetermined phase-shifted angle α. As shown in Fig. 9, mutual inductances M_{13} and M_{24} are both positive throughout the misalignment range. From (4) and (19), coupling coefficients k_{15} or k_{25} are positive or negative when currents i_{s1} and i_{s3} or i_{s2} and i_{s3} are in phase or out of phase. Based on predetermined coupling references for k_{15} and k_{25}, the coil position quadrant can be determined.

C. Air Gap Distance Determination

The coil position can be determined based on the above sensing processes given a specific vertical distance between the transmitter and receiver pads. In practice, the air gap distance can vary over several centimeters due to various vehicle loading cases or primary coil mounting arrangements. A separate positioning strategy should be explored to adapt to this variation. Here, an air gap distance range from 170 to 210 mm is explored based on an actual EV prototype.

From the intersection point determination method in part *A*, coupling coefficients k_{13} and k_{24} can still be calculated from (16) and (17) with a different air gap distance. Misalignment characteristics in Fig. 3 will increase overall. As shown in Figs. 13 and 14, air gap distances of 180 and 210 mm were selected to demonstrate intersection point movements. Four intersection lines and eight intersection points can be determined. In Fig. 13, dotted lines 1 and 2 behave identically to those in Fig. 9. Dotted lines 3 and 4 are intersections between a fixed 0.19 coupling surface and coupling surfaces of k_{13} and k_{24} with a 180 mm air gap distance. The dotted lines 1–4 in Fig. 13 are replotted in Fig. 14(a). Another case with k_{13} and k_{24} calculated as 0.2 and 0.16 is shown in Fig. 14(b). The symmetry of lines 1–4 results in symmetrical positions of points *A*–*D* and *A*′–*D*′. These

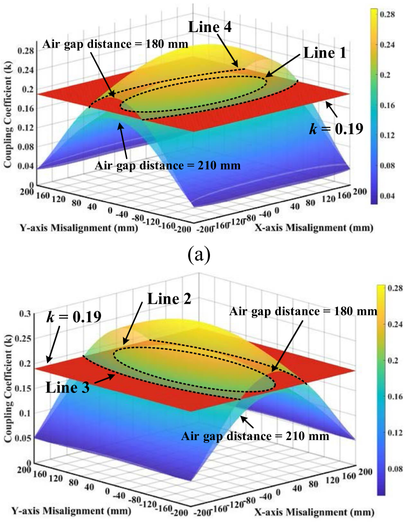

(a)

(b)

Fig. 13. Coupling coefficients of (a) k_{13} and (b) k_{24} for various misalignment cases with a fixed coupling coefficient of 0.19 and air gap distances of 210 and 180 mm.

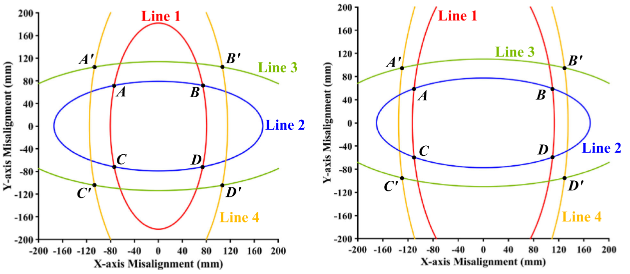

(a) (b)

Fig. 14. Intersection lines 1–4 in one two-dimensional plane with 210 and 180 mm air gap distances. (a) $k_{13} = 0.19$ and $k_{24} = 0.19$. (b) $k_{13} = 0.2$ and $k_{24} = 0.16$.

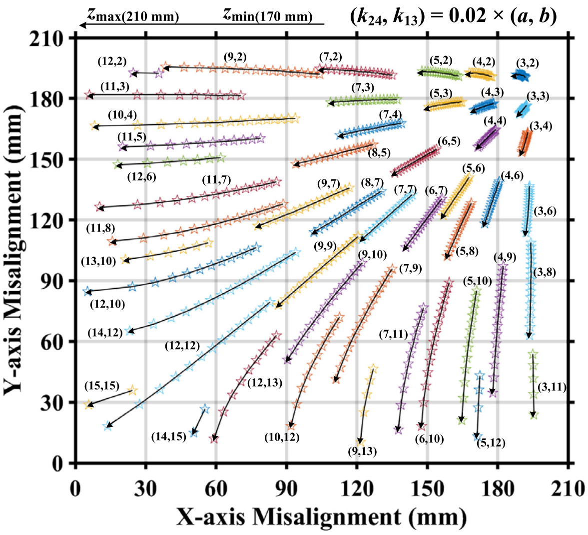

Fig. 15. Loci of intersection points in the first quadrant for various air gap distances and various coupling coefficient pairs. The air gap distance varies from 170 to 210 mm. Notations in the brackets multiplied by 0.02 represent coefficient pairs (k_{24}, k_{13}).

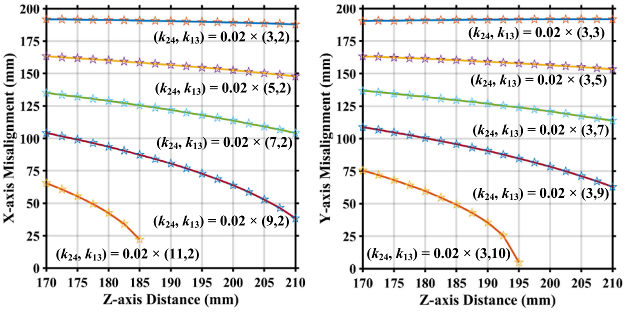

(a) (b)

Fig. 16. Loci of intersection points in the first quadrant for various z-axis air gap distances and various coupling coefficient pairs. (a) Projections onto the xz-plane. (b) Projections onto the yz-plane.

points are distributed across four quadrants. Their coordinates can be calculated by polynomial fits as in (18). From the quadrant determination method in part *B*, points in different quadrants can be disambiguated.

To distinguish intersection points in one quadrant, such as *B* and *B*′, the first quadrant is taken as an example. As shown in Fig. 15, each pair of coupling coefficients (k_{24}, k_{13}) corresponds to a set of points. Each point is a potential position for one air gap distance. To illustrate this, 17 air gap distance values from 170 to 210 mm with 2.5 mm intervals were selected. From part *A*, 17 pairs of polynomial fits as in (18) were prepared and 17 coordinates were calculated. These coordinates act as intersection points as in Fig. 14. The points close to and away from the origin correspond to respective long and short air gap distances. In total, ten coefficient pairs of (k_{24}, k_{13}) in Fig. 15 are demonstrated in Fig. 16 with these 17 air gap distances. It should be noted that some lines in Figs. 15–16 have less than 17 points. For example, the air gap distance range for the coefficient pair (0.22, 0.04) in Fig. 16(a) is from 170 to 185 mm. For these cases, the air gap distance range decreases but is still monotonic.

To distinguish the specific position along one intersection point locus, the auxiliary square coil 5 on the secondary side is reused. The rms value of current i_{s3} should be measured. Similar to the operation in Fig. 8, coupling coefficients k_{15} and k_{25} can be calculated as

$$k_{15}, k_{25} \approx \frac{L_{\mathrm{C}}}{\sqrt{L_{\mathrm{TR}} L_{\mathrm{s3}}}} \frac{I_{\mathrm{s3-1,s3-2}} R_{\mathrm{L}}{}'}{(V_{\mathrm{in}} - 2 I_{\mathrm{in1}} R_{\mathrm{ds(on)}})} \frac{1}{\cos(\alpha/2)} \frac{\pi}{2\sqrt{2}} \tag{20}$$

where $I_{\text{s3-1}}$ and $I_{\text{s3-2}}$ are measured as in Fig. 8(a) and (b), respectively.

Coefficients k_{15} and k_{25} are related to the dimensions of coil 5. In Fig. 17, the sums of k_{15} and k_{25} for diagonal misalignment cases and various lengths of square coil 5 are presented. This characteristic should be monotonic. The length is designed to be 260 mm.

A top view of secondary pad structures with coil 5 is shown in Fig. 18. Based on the length selection, the sum of coefficients k_{15} and k_{25} for various misalignment cases with 180 and 210 mm air gap distances is shown in Fig. 19. The coupling variation

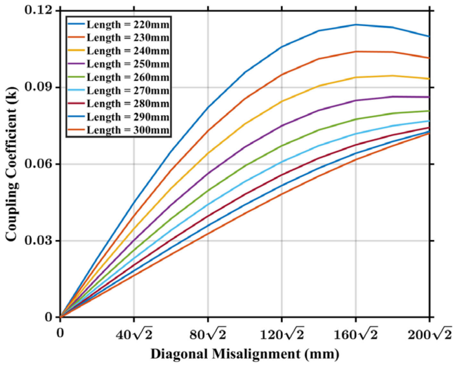

Fig. 17. Sum of coupling coefficients k_{15} and k_{25} for diagonal misalignment cases and various lengths of square coil 5.

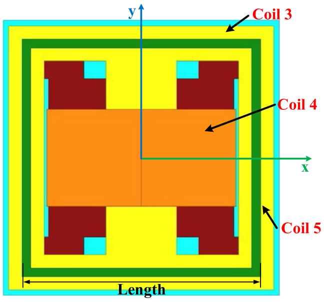

Fig. 18. Top view of secondary pad structures with coil 5.

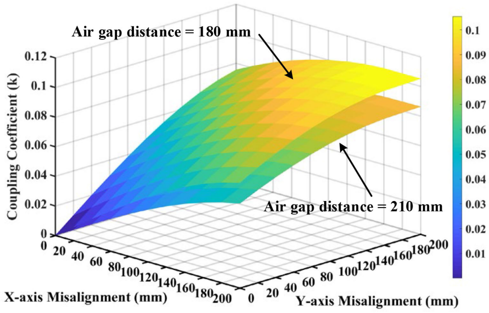

Fig. 19. Sum of coupling coefficients k_{15} and k_{25} for various misalignment cases with 210 and 180 mm air gap distances.

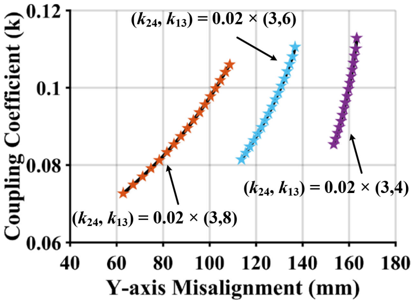

Fig. 20. Sum of coupling coefficients k_{15} and k_{25} for points with coefficient pairs (0.06, 0.08), (0.06, 0.12), and (0.06, 0.16).

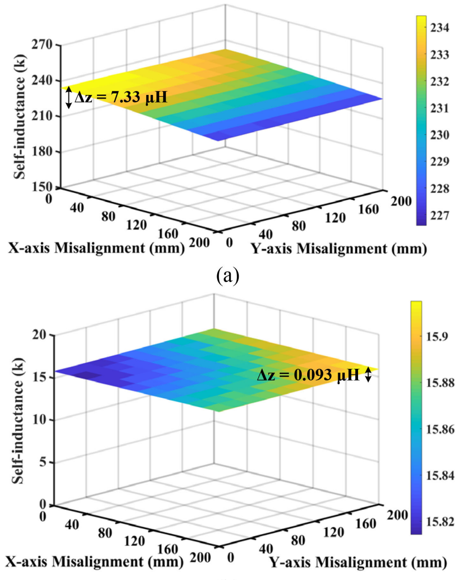

(a)

(b)

Fig. 21. Coil self-inductance of (a) L_{TR} and (b) L_{s3} for various misalignment cases with a 210 mm air gap distance.

tendency is monotonic along the diagonal direction. This is similar to the intersection point loci shown in Figs. 15 and 16. Consequently, points close to the origin represent long air gap distances and low $k_{15} + k_{25}$ values. Points away from the origin represent short air gap distances and high $k_{15} + k_{25}$ values. As shown in Fig. 20, each point with coefficient pairs (0.06, 0.08), (0.06, 0.12), and (0.06, 0.16) matches a unique $k_{15} + k_{25}$ value. The coil position can be determined from this result.

Misalignment between transmitter and receiver coils causes coupling coefficient and self-inductance variations. From (20), current I_{s3} and the product of self-inductances L_{TR} and L_{s3} will change with misalignment and will lead to k_{15} and k_{25} errors. Simulation results of L_{TR} and L_{s3} for various misalignment cases are shown in Fig. 21. Their maximum variation ranges are 7.33 and 0.093 μH with a 210-mm air gap. The ranges increase to 13.64 and 0.16 μH considering a 40-mm air gap variation. These are 5.6% and 1.1% of their nominal values. In this case, the maximum variation of the square root of the product of L_{TR} and L_{s3} is 2.3%. Corresponding maximum variation of current I_{s3} due to the detuning state is 2% from simulations. Their variation directions are both downward. This helps to reduce errors in k_{15} and k_{25}. The errors can be computed from (20) and are approximately 0.29%.

Self-inductance variation is usually minor for static EV charging applications because of long air gaps. However, system parameters should be designed carefully for IPT applications with small air gaps, such as rail transportation. The self-inductance variation can be substantial in such cases [34].

The flowchart in Fig. 22 summarizes practical procedures of the proposed coil positioning method. First, communications between the vehicle and charging station are established. Next, the DD coil inverter is activated with a 50% duty ratio or a predetermined phase-shifted angle α as in Fig. 8(a). The output voltage V_{o1}, resonant current I_{s3}, and phase relationships between currents i_{s1} and i_{s3} are measured on the vehicle. After the charging station receives a completion signal, the solenoidal coil inverter is activated as in Fig. 8(b). The output voltage V_{o2},

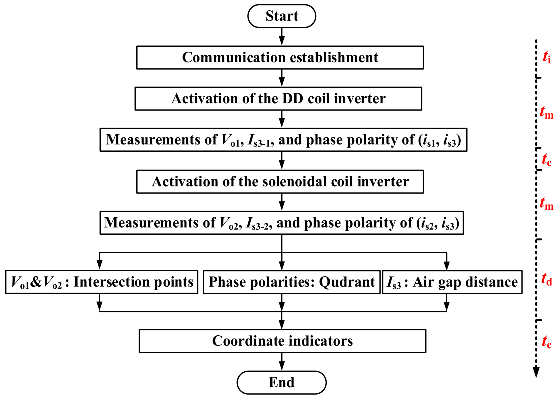

Fig. 22. Practical procedures of the proposed coil positioning method.

resonant current I_{s3}, and phase relationships between currents i_{s2} and i_{s3} are measured. In terms of principles in parts *A*–*C*, four intersection points loci distributed across four quadrants can be obtained from V_{o1} and V_{o2}. The actual position quadrant can be determined based on current phase relationships. The specific position can be determined after these procedures from I_{s3} measurements. It is worth noticing that the method also works when the secondary pad is exactly on the *x* and *y* axes. From the results, coordinate indicators are provided to the charging station for misalignment compensation. Calibrated coefficients and their polynomial fit results can be saved in a lookup table in advance.

Communications are required for the proposed positioning method. The time needed for the complete positioning process is identified in Fig. 22, and is

$$t = 2t_{\mathrm{c}} + 2t_{\mathrm{m}} + t_{\mathrm{d}} \tag{21}$$

where t_{c} represents the time for communication and message passing between the vehicle and charging station, t_{m} represents the time for signal processing and ADC sampling, and t_{d} represents the time for logical operations and coordinate calculations. Their typical values are given in the experimental results. It should be noted that the time t_{i} for communication establishment is not included.

V. EXPERIMENTAL RESULTS

A 3.2-kW IPT charging system prototype with *LCC* series compensation and an IPOS circuit structure was built and tested to demonstrate the feasibility of the proposed NRS transformer. A photograph of the transformer pad is shown in Fig. 23(a). DD and solenoidal coils are arranged orthogonally, matching the dimensions in Table I. The transmitter and receiver coil and ferrite core arrangements are identical except for the addition of coil 5. Cross-coupling coefficients k_{14} and k_{23} are less than 0.01, consistent with the analysis. A photograph of the experimental prototype is shown in Fig. 23(b). The IPT system consists of two H-bridge inverters, the primary and secondary transformer pads with their compensation components, two diode rectifiers, and load resistances. Measured parameters of resonant components are listed in Table III. A Chroma dc source (62100H-450) provides the input power, nominally 300 V. Two SiC MOSFET modules (SK45MH120TSCp) from Semikron are used for the inverters and SiC Schottky diodes are used for the rectifiers. Resonant inductors use PQ 50/50 ferrite cores. Polypropylene film capacitors in series and parallel combinations are used as compensation components. The system controller is implemented with a Texas Instruments TMS320F28335 DSP to generate inverter switching signals. The operating frequency is set to 85 kHz. The nominal load resistance is 50 Ω.

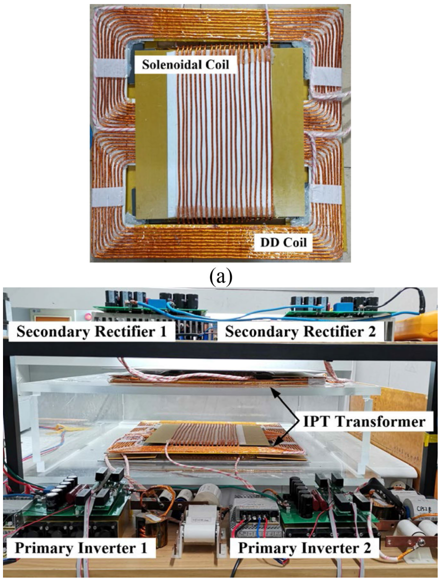

(a)

(b)

Fig. 23. (a) NRS transformer. (b) 3.2-kW IPT experimental prototype.

TABLE III
MEASURED RESONANT TANK PARAMETERS

Parameters	Symbols	Values
Transmitter DD coil inductance	L_{p1}	238.5 μH
Transmitter solenoidal coil inductance	L_{p2}	224.9 μH
Receiver DD coil inductance	L_{s1}	233.0 μH
Receiver solenoidal coil inductance	L_{s2}	237.3 μH
Primary resonant capacitors	C_{p1}/C_{p2}	21.51/23.53 nF
	C_{p3}/C_{p4}	46.85/46.96 nF
Primary resonant inductors	L_{p3}/L_{p4}	75.46/75.78 μH
Secondary resonant capacitors	C_{s1}	14.71 nF
	C_{s2}	15.57 nF
	C_{s3}	0.185 μF
Resonant frequency	f_s	85 kHz

Experimental results for coupling coefficients k_{13}, k_{24}, k_{14}, and k_{23} given various misalignment cases in the first quadrant are shown in Fig. 24(a)–(d). An array of 7 × 7 test points was measured. Coupling results in the other three quadrants are symmetric. From Fig. 24, measured coupling coefficients are slightly less than those in the simulations. The deviations are less than 5%. Minor differences are due to simplifications of the transformer model and dimensional tolerances in the actual prototype. In the tests, k_{13} behaves better for *x*-axis misalignment and k_{24} has more impact for *y*-axis misalignment. Directional selectivity characteristics were confirmed. Across a defined narrow misalignment range, here ±60 mm for both *x*

TABLE IV
FITTING COEFFICIENTS FOR DD AND SOLENOIDAL COIL MISALIGNMENT

Coefficients	p_{00}	p_{10}	p_{01}	p_{20}	p_{11}	p_{02}	p_{30}	p_{21}	p_{12}	p_{03}
DD coils	0.2176	1.008×10^{-5}	-2.621×10^{-5}	-1.390×10^{-6}	-8.960×10^{-7}	-6.689×10^{-6}	8.635×10^{-11}	7.248×10^{-9}	3.231×10^{-9}	9.850×10^{-9}
Solenoidal coils	0.2132	3.264×10^{-5}	4.134×10^{-5}	-6.764×10^{-6}	-1.294×10^{-6}	-1.647×10^{-6}	1.179×10^{-8}	5.928×10^{-9}	6.100×10^{-9}	1.759×10^{-9}

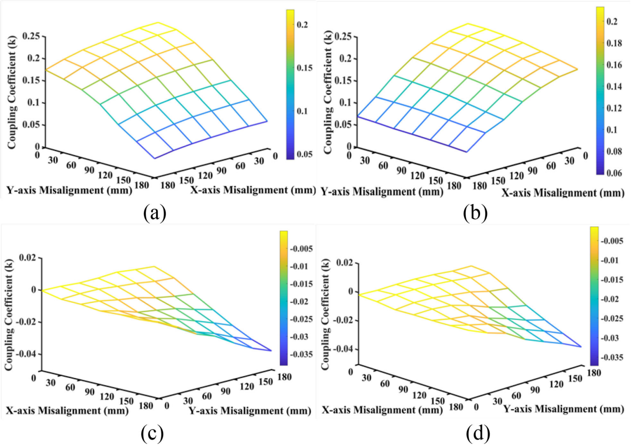

Fig. 24. Measured coupling coefficients of (a) k_{13}, (b) k_{24}, (c) k_{14}, and (d) k_{23} for various misalignment cases.

and *y* directions, absolute values of k_{14} and k_{23} do not exceed 0.01. This validates the circuit simplifications of (9) and (10).

A. Preactivation Sensing Process

The position sensing process is carried out before activation of the power paths, following the discussion in Section IV. When air gap distance is fixed, a two-step procedure is implemented. When air gap variation is considered, a three-step procedure is required. Based on these, experimental verification will be divided into two parts. Coupling results in the first quadrant will be presented as examples.

When the air gap is fixed at 210 mm, polynomial fits for coupling coefficients k_{13} and k_{24} can be obtained with the *cftool* MATLAB toolbox based on Fig. 3(a) and (b). Fitting results follow (18) and coefficients are listed in Table IV. Four digits are retained to help preserve fit precision, although most of the electrical measurements have a resolution of about 1%. *R*-square values of the respective fits are 0.9995 and 0.9997. Coupling coefficient calibrations from simulation results and polynomial fitting results are shown in Fig. 25.

Various points distributed throughout the ±180 mm × 180 mm range with a fixed 210-mm air gap were tested to verify the proposed coil positioning method. As shown in Fig. 26, square and triangular points represent calibration values and test results. The secondary pad was placed at marked positions and the position sensing process was carried out. At each point, circuit output voltages V_{o1} and V_{o2} were measured and intersection point coordinates were calculated. From Fig. 26, the proposed method shows high positioning accuracy. Among the 49 tested locations, 92% are accurate to within 10 mm. The average *x*-axis and *y*-axis deviations were 3.27 and 2.70 mm.

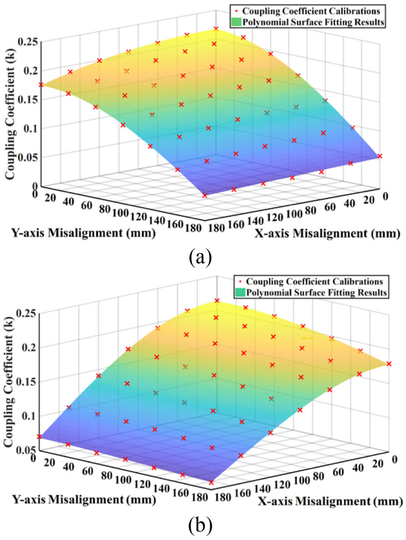

Fig. 25. Coupling coefficient calibrations and polynomial fits for (a) k_{13} and (b) k_{24}.

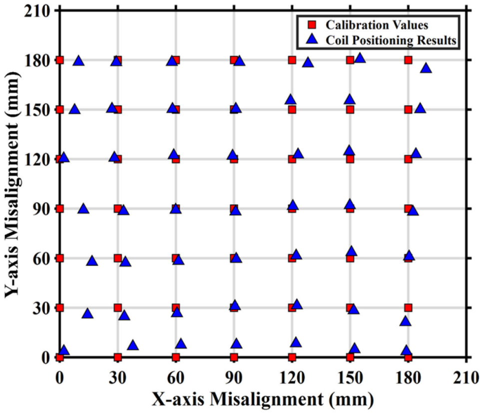

Fig. 26. Coil positioning results for points distributed throughout the 180 mm × 180 mm range with a 210 mm air gap distance.

These residual errors reflect measurement accuracy limits of coupling coefficients, truncation and fitting errors, and the use of approximate circuit relations (16) and (17). In (16) and (17), $R_{\mathrm{ds(ON)}}$ of MOSFETs is used as a parameter. $R_{\mathrm{ds(ON)}}$ changes with temperature for a given gate–source voltage V_{gs}. For the SiC MOSFET module used here, $R_{\mathrm{ds(ON)}}$ is 45 mΩ at 25 °C and 76 mΩ at 150 °C junction temperatures. This results in up to 0.2 V variation in V_{p}. The coupling coefficient error, computed from (16) and (17), is less than 0.1%.

For quadrant determination, phase shifts among i_{s1}, i_{s2}, and i_{s3} were measured using the circuit shown in Fig. 27. The current transducers have galvanic isolation. A multiplier circuit and LPF

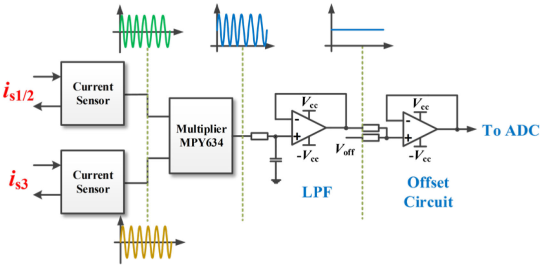

Fig. 27. Circuit diagram for phase polarity measurements.

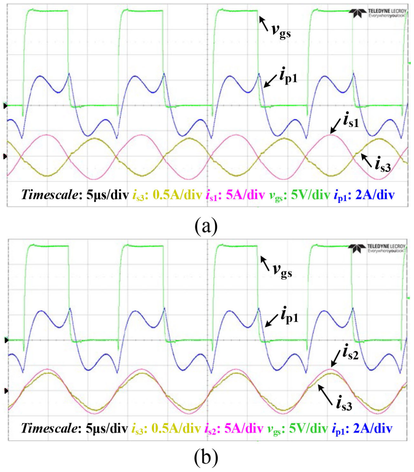

(a)

(b)

Fig. 28. Experimental waveforms of the IPT system for phase measurement with the activation of inverter (a) in the first power transmission path and (b) in the second power transmission path.

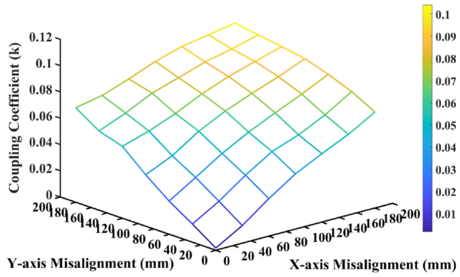

Fig. 29. Measured coupling coefficients of the sum of k_{15} and k_{25} for various misalignment cases.

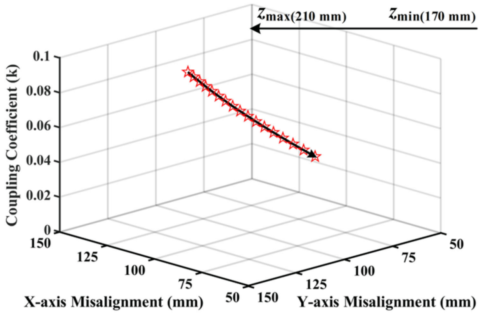

Fig. 30. Sum of coupling coefficients k_{15} and k_{25} for points with coefficient pairs (0.1858, 0.1598).

(low-pass filter) were employed to obtain relative phase shifts. The filter output voltage is positive when the input currents are approximately in phase and negative when they are out of phase. A level shifter ensures that the ADC signal voltage is within range. Only phase polarities between i_{s1} and i_{s3} or i_{s2} and i_{s3}, rather than specific phase angles, are required for quadrant determination, as shown earlier. This adds robustness. Short current sensor time delays or decreased phase measurement accuracy have little impact since the multiplier acts in a manner similar to averaging differences.

To verify the quadrant determination method, a position with 60 mm x-axis and -60 mm y-axis misalignment serves as an example. The experimental waveforms for this point are shown in Fig. 28. Resonant currents i_{s1} and i_{s3} are out of phase. Resonant currents i_{s2} and i_{s3} are in phase. Based on predetermined coupling and current references, the position must be in the second quadrant.

When air gap variation is considered, an air gap determination process is required. As in Fig. 25 and Table IV, 17 pairs of polynomial fits for coupling coefficients k_{13} and k_{24} were obtained with 17 air gap values. The values spanned 170 to 210 mm in 2.5 mm intervals, as in Fig. 15. Sum results of k_{15} and k_{25} were also recorded.

To verify the proposed method, various position points distributed throughout the ±180 mm × 180 mm range with a fixed air gap distance were tested. The air gap distance was treated as unknown before the procedures (it had been set to 180 mm). For each point, coupling coefficients k_{13}, k_{24}, k_{15}, and k_{25} were measured as in (16), (17), and (20). From the k_{13} and k_{24} results, 49 intersection point loci were obtained as in Fig. 15. Each point is a potential position for one air gap distance. From (20), i_{s3} can be measured using an rms-to-dc converter such as AD637. Experimental results for the sum of k_{15} and k_{25} given various misalignment cases are shown in Fig. 29. In terms of coefficients in Fig. 29, the specific air gap distances and three-dimensional coordinates for each point can be determined.

The point (120 mm, 90 mm, 180 mm) was selected to elaborate the above process. Coupling coefficients k_{13}, k_{24}, and $k_{15} + k_{25}$ were measured as 0.1858, 0.1598, and 0.7869. From the k_{13} and k_{24} values, an intersection point locus can be obtained, as in Fig. 15. The locus is shown in Fig. 30. Each point on the locus corresponds to a unique $k_{15} + k_{25}$ value. The computed point was (122.71 mm, 93.98 mm, 181.82 mm). The other 48 points can be tested using the same procedures.

Similar to Fig. 26, calibration values are shown as squares and experimental test results as triangles in Fig. 31. The proposed method maintains accuracy when air gap distance variations are taken into consideration. Among the 49 tested locations, 84% are accurate to within 10 mm and 90% are accurate to within 12 mm. The average x-axis and y-axis deviations were 4.34 and 5.55 mm. An error of 12 mm within the power charging range leads to a maximum 4% variation of the main coupling coefficients. From (2) and (9), resonance can be maintained, although voltage gain will vary accordingly. As in Fig. 30, z-axis deviations of test results in Fig. 31 were calculated and are listed in Table V. The row and column headings correspond to x and y-axis coordinates

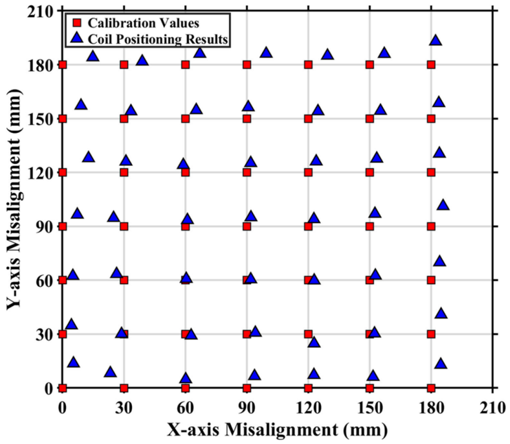

Fig. 31. Coil positioning results for points distributed throughout the 180 mm × 180 mm range with a 180 mm air gap distance.

TABLE V
TEST RESULTS, *Z*-AXIS DEVIATIONS, ALL IN MILLIMETERS

x \ *y*	0	30	60	90	120	150	180
0	+4.13	+3.88	+2.85	+1.65	+1.89	+2.12	-1.21
30	+2.32	+1.85	+1.93	+1.79	+2.23	-3.81	-3.45
60	+2.93	+2.02	+2.84	+3.15	+2.62	-0.05	-4.72
90	+2.53	+2.22	+2.19	+2.59	+1.82	-0.26	-6.41
120	-0.96	+0.50	+3.07	+2.35	+0.97	-1.38	-6.78
150	+0.29	+0.62	+0.52	+0.19	-1.04	-2.30	-8.57
180	-1.29	-1.20	-6.07	-3.18	-6.17	-8.22	-9.91

for a set 180 mm z value. The average absolute value of z-axis deviation was 2.79 mm.

For the positioning process, a typical value of t_c is 5.5 ms when transferring 5 bytes with a 9600 baud rate. A typical value of t_m is 3 μs for ADC sampling and software filtering and 200 ms for the system to achieve a steady output. In practice, the calibrated coupling coefficients should be measured in advance. Multiple fit results as in Table IV would be calculated and saved in a lookup table. In the actual preactivation sensing process, numerical solutions of intersection coordinates in (18) can be solved in real time using Newton's method in the DSP. For the 17 air gap test values, the typical value of t_d was 100 ms. The total time t needed for the complete process can be estimated as 0.52 s.

B. Power Transfer Stage

In a practical system, the power transfer stage should be activated only when the vehicle is brought into the defined narrow misalignment range, such as during parking. Experimental results for system output characteristics and dc–dc conversion efficiency given various load resistances with a 210 mm air gap distance are shown in Fig. 32(a) and (b). From Fig. 32(a), the output voltages of each power path stay close to 200 V. An operating model based on an approximate voltage-source output therefore is confirmed to be appropriate. The maximum voltage deviation shows less than 3% error due largely to the parasitic resistances. From Fig. 32(b), the nominal output power is close to 3 kW and power decreases to 530 W at the 290 Ω light-load resistance condition. The maximum system efficiency is 94.6% at nominal output power and decreases to 91.0% at 530-W output.

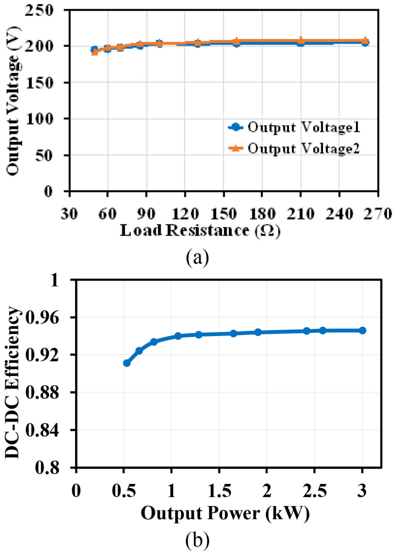

(a)

(b)

Fig. 32. (a) System output characteristics and (b) dc–dc conversion efficiency for various load resistances.

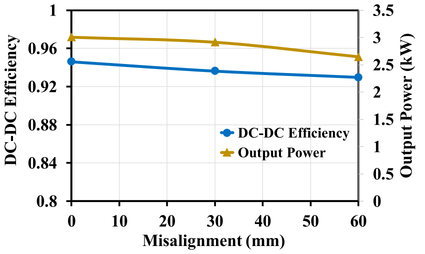

Fig. 33. System output characteristics and dc–dc conversion efficiency for lateral misalignment.

Experimental results given lateral misalignment are shown in Fig. 33. For these misalignment cases, the load resistance is held at 50 Ω. Output power and efficiency decrease as the coupling coefficient decreases. The minimum system efficiency is 93.0% for 60-mm lateral misalignment with the nominal load.

Experimental waveforms for various load resistances and misalignment cases are shown in Fig. 34. Voltages v_{gs} and v_{ds} are measured for one MOSFET in the inverter. Primary resonant currents i_{p1} and i_{p2} are also shown. Current magnitudes decrease as the coupling coefficient decreases and as the load resistance increases. Detailed views of transistor turn-ON are also shown in Fig. 34, demonstrating that soft-switching conditions are met and that ZVS operation is achieved for various load and misalignment cases.

VI. DISCUSSION AND COMPARISONS

Conventional IPT systems consist of a single pair of coils on transmitter and receiver pads. To implement a high-power

TABLE VI
COMPARISONS OF POSITIONING STRATEGIES

Methods	Auxiliary sensors and circuits	Auxiliary coils	Auxiliary sources	Misalignment types and ranges	Main transformer Dimensions
[22]	12 single-axis TMR2001 sensors and circuits (*Aux.*)	None	None	A_1: ±50 mm, radial misalignment A_2 & A_3: None	90 mm diameter, circular 30 mm air gap distance
[23]	14 × 14 matrix TMR2001 sensors and circuits (*Aux.*)	None	None	A_1: ±150 mm × 150 mm misalignment A_2 & A_3: None	200 mm × 200 mm, square 100 mm air gap distance
[24]	4 symmetrical hall sensors (SS491B) and circuits (*Aux.*)	None	A 6 A dc current source with a relay	A_1: ±100 mm × 80 mm misalignment A_2 & A_3: None	250 mm diameter, circular 60 mm air gap distance
[25]	4 voltage sensing circuits (*Aux.*)	4 circular coils	None	A_1: ±700 mm × 100 mm misalignment A_2: 90 mm - 140 mm misalignment A_3: None	560 mm diameter, circular Max 140 mm air gap distance
[26]	4 voltage sensing circuits (*Aux.*)	4 circular coils	None	A_1: ±100 mm × 100 mm misalignment A_2 & A_3: None	550 mm × 550 mm, square 200 mm air gap distance
[27]	16 voltage sensing circuits (*Aux.*)	16 non-overlapping coil sets	None	A_1: ±600 mm, x-axis misalignment only A_2: 50 mm - 200 mm misalignment A_3: None	600 mm × 440 mm, rectangular Max 200 mm air gap distance
[28]	1 voltage sensing circuit (*Aux.*)	3 circular coils	A dc voltage source with 3 relays	A_1: ±90 mm, radial misalignment A_2: 100 mm - 110 mm misalignment A_3: None	200 mm diameter, circular Max 110 mm air gap distance
Proposed method	2 Hall voltage sensors and circuits (*Shared*) 3 current transducers and circuits (*Aux.*)	1 square coil	None	A_1: ±200 mm × 200 mm misalignment A_2: 170 mm - 210 mm misalignment A_3: None	600 mm × 600 mm, square Max 210 mm air gap distance

Note: A_1 refers to horizontal misalignment (x and y axes). A_2 refers to vertical misalignment (z-axis). A_3 refers to rotational misalignment. *Aux.* refers to auxiliary sensors and circuits for positioning. *Shared* refers to sensors and circuits shared for both positioning and system power control targets.

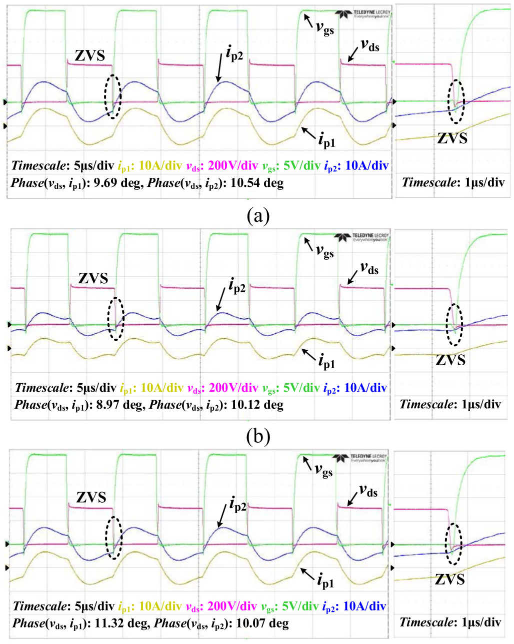

(a)

(b)

(c)

Fig. 34. Experimental waveforms of the IPT system and detailed views on zero voltage switching (ZVS) transitions. (a) Fully aligned ($R_L = 50\ \Omega$). (b) Fully aligned ($R_L=100\ \Omega$). (c) At 60 mm x-axis and 60 mm y-axis misalignment ($R_L = 50\ \Omega$).

IPT system, multiple power channels in parallel are an effective approach to upgrade system power capacity. The approach is preferred because low-power and low-cost semiconductors and passive components can be employed with identical voltage or current tolerances [8]–[13], [35]–[37]. Multiple power channels require transformers with multiple transmitters and multiple receivers. To deal with this issue, an NRS structure has been proposed in Fig. 1, composed of a pair of DD coils and a pair of solenoidal coils. The coils are integrated spatially and decoupled magnetically. Two independent power transmission paths were prepared using an IPOS circuit structure in Fig. 5. Compared to a single power path with full capacity, the current capacity of MOSFETs and passive components on the primary side can be reduced by half. The voltage capacity of diodes on the secondary side can be reduced by half. The device tolerance results in advantages of better system compatibility and higher flexibility, although total system cost and volume can be higher with double component counts. Integrated transformers do not add extra space. Compared to previous two-channel system designs [8]–[10], the proposed NRS structure can achieve positioning targets with less auxiliary sensors, coils, and sources. This adds system reliability and decreases complexity and cost for positioning. Therefore, the proposed design has potential significance for practical implementation when a multichannel structure and position compensation are involved.

Table VI reviews and compares a variety of coil positioning strategies. Auxiliary tunneling magnetoresistive (TMR) and Hall sensors were adopted in [22]–[24] to determine coil positioning considering horizontal misalignment only. Vertical misalignment was not considered. The sensors have a lower cost than cameras, RFIDs, radar, and optical sensors. The required sensor count is high and sensor positions are of great importance to positioning precision. For the methods in [25]–[28], auxiliary coils were employed. Multiple voltage sensing circuits were needed to measure induced auxiliary coil voltages. Vertical misalignment was not considered in [26]. Only x-axis misalignment was investigated in [27]. An additional voltage source and three relays were required in [28].

Compared to [25], the proposed method can compensate for a higher maximum air gap with fewer auxiliary coils and almost identical transformer dimensions. Two Hall-effect sensors and three 2000:1 current transducers were used for the proposed positioning method. The current transducers were employed for i_{s1}, i_{s2}, and i_{s3} measurements. Output voltage sensors were shared for both positioning and system power control targets.

Based on these comparisons, there is only one power channel for previous methods [22]–[28]. One set of inverters and rectifiers was used. The methods distinguish power transfer and positioning targets. Auxiliary sensors, coils, and sources were added to the systems to extract position information. For the proposed method, output voltages and secondary resonant currents are obtained mainly from the power paths. Inverter and rectifier counts are twice those in systems with one power channel. The method has merits of less auxiliary equipment, higher compatibility, and higher positioning ranges considering both horizontal and vertical misalignment cases. One possible drawback of the proposed method is the use of power channels, although the use of multiple power channels has device tolerance advantages as discussed above.

In practical EV applications, high angular misalignment is less likely to occur [27], [38]. The methods in Table VI cannot distinguish this type of misalignment. When there are both air gap variations and rotational misalignment, the positioning strategy will be more complicated. This is an opportunity for further research.

VII. CONCLUSION

In this article, a secondary coil positioning method integrated with an orthogonal decoupled transformer is proposed. Using an IPOS circuit structure and an auxiliary secondary square coil, two transmission paths are activated separately before power path activation. Both horizontal and vertical misalignment can be distinguished with high positioning accuracy. Compared to prior positioning methods, the proposed method has the advantages of less auxiliary equipment, higher compatibility, and higher positioning ranges. A 3.2-kW prototype was implemented and demonstrated the feasibility of the proposed positioning method. Experimental results show that 92% of tested points are accurate to within 10 mm with a 210 mm air gap distance. When air gap distance variations are taken into consideration, 90% of tested points are accurate to within 12 mm. The proposed design supports a multichannel structure and accurate position compensation.

ACKNOWLEDGMENT

The authors would like to thank Principal Supervisors H. Ma, D. Xu, and P. Krein.

REFERENCES

[1] G. A. Covic and J. T. Boys, “Inductive power transfer,” *Proc. IEEE*, vol. 101, no. 6, pp. 1276–1289, Jun. 2013.

[2] S. Li and C. C. Mi, “Wireless power transfer for electric vehicle applications,” *IEEE J. Emerg. Sel. Topics Power Electron.*, vol. 3, no. 1, pp. 4–17, Mar. 2015.

[3] D. Patil, M. K. McDonough, J. M. Miller, B. Fahimi, and P. T. Balsara, “Wireless power transfer for vehicular applications: Overview and challenges,” *IEEE Trans. Transp. Electrific.*, vol. 4, no. 1, pp. 3–37, Mar. 2018.

[4] A. Zaheer, H. Hao, G. A. Covic, and D. Kacprzak, “Investigation of multiple decoupled coil primary pad topologies in lumped IPT systems for interoperable electric vehicle charging,” *IEEE Trans. Power Electron.*, vol. 30, no. 4, pp. 1937–1955, Apr. 2015.

[5] M. Budhia, J. T. Boys, G. A. Covic, and C. Y. Huang, “Development of a single-sided flux magnetic coupler for electric vehicle IPT charging systems,” *IEEE Trans. Ind. Electron.*, vol. 60, no. 1, pp. 318–328, Jan. 2013.

[6] A. Tejeda, S. Kim, F. Lin, G. A. Covic, and J. T. Boys, “A hybrid solenoid coupler for wireless charging applications,” *IEEE Trans. Power Electron.*, vol. 34, no. 6, pp. 5632–5645, Aug. 2018.

[7] D. Ahn and S. Hong, “Effect of coupling between multiple transmitters or multiple receivers on wireless power transfer,” *IEEE Trans. Ind. Electron.*, vol. 60, no. 7, pp. 2602–2613, Jul. 2013.

[8] H. Liu, Q. Che, G. Ke, X. Ren, and S.-C. Wong, “Research of the input-parallel output-series inductive power transfer system,” in *Proc. IEEE PELS Workshop Emerg. Technol., Wireless Power*, Jun. 2015, pp. 1–7.

[9] T. Shijo *et al.*, “EMI reduction technology in 85 kHz band 44 kW wireless power transfer system for rapid contactless charging of electric bus,” in *Proc. IEEE Energy Convers. Congr. Expo.*, Sep. 2016, pp. 1–6.

[10] Y. Li *et al.*, “Efficiency analysis and optimization control for input-parallel output-series wireless power transfer systems,” *IEEE Trans. Power Electron.*, vol. 35, no. 1, pp. 1074–1085, Jan. 2020.

[11] G. A. J. Elliott, S. Raabe, G. A. Covic, and J. T. Boys, “Multiphase pickups for large lateral tolerance contactless power-transfer systems,” *IEEE Trans. Ind. Electron.*, vol. 57, no. 5, pp. 1590–1598, May 2010.

[12] G. Ke, Q. Chen, W. Gao, S. Wong, C. K. Tse, and Z. Zhang, “Research on IPT resonant converters with high misalignment tolerance using multi-coil receiver set,” *IEEE Trans. Power Electron.*, vol. 35, no. 4, pp. 3697–3712, Apr. 2020.

[13] S. Y. Jeong, S. Y. Choi, M. R. Sonapreetha, and C. T. Rim, “DQ quadrature power supply coil sets with large tolerances for wireless stationary EV chargers,” in *Proc. IEEE PELS Workshop Emerg. Technol., Wireless Power*, Jun. 2015, pp. 1–6.

[14] G. Ke, Q. Chen, L. Xu, X. Ren, and Z. Zhang, “Analysis and optimization of a double-sided S-LCC hybrid converter for high misalignment tolerance,” *IEEE Trans. Ind. Electron.*, vol. 68, no. 6, pp. 4870–4881, Jun. 2021.

[15] J. L. Villa, J. Sallan, J. F. Sanz Osorio, and A. Llombart, “High-misalignment tolerant compensation topology for ICPT systems,” *IEEE Trans. Ind. Electron.*, vol. 59, no. 2, pp. 945–951, Feb. 2012.

[16] J. Zhao, T. Cai, S. Duan, H. Feng, C. Chen, and X. Zhang, “A general design method of primary compensation network for dynamic WPT system maintaining stable transmission power,” *IEEE Trans. Power Electron.*, vol. 31, no. 12, pp. 8343–8358, Dec. 2016.

[17] L. Zhao, D. J. Thrimawithana, and U. K. Madawala, “Hybrid bidirectional wireless EV charging system tolerant to pad misalignment,” *IEEE Trans. Ind. Electron.*, vol. 64, no. 9, pp. 7079–7086, Sep. 2017.

[18] F. Lu, H. Zhang, H. Hofmann, W. Su, and C. C. Mi, “A dual-coupled LCC-compensated IPT system with a compact magnetic coupler,” *IEEE Trans. Power Electron.*, vol. 33, no. 7, pp. 6391–6402, Jul. 2018.

[19] *Wireless Power Transfer for Light-Duty Plug-in/Electric Vehicles and Alignment Methodology*, Standard J2954_201904, 2019. [Online]. Available: http://saemobilus.sae.org/content/J2954_201904/

[20] J. Tiemann, J. Pillmann, S. Bocker, and C. Wietfeld, “Ultra-wideband aided precision parking for wireless power transfer to electric vehicles in real life scenarios,” in *Proc. IEEE Veh. Technol. Conf.*, Sep. 2016, pp. 1–5.

[21] W. Shieh, C. J. Hsu, and T. Wang, “Vehicle positioning and trajectory tracking by infrared signal-direction discrimination for short-range vehicle-to-infrastructure communication systems,” *IEEE Trans. Intell. Transp. Syst.*, vol. 19, no. 2, pp. 368–379, Feb. 2018.

[22] W. Han, K. T. Chau, C. Jiang, and W. Liu, “Accurate position detection in wireless power transfer using magnetoresistive sensors for implant applications,” *IEEE Trans. Magn.*, vol. 54, no. 11, Nov. 2018, Art. no. 4001205.

[23] X. Liu, C. Liu, W. Han, and P. W. T. Pong, “Design and implementation of a multi-purpose TMR sensor matrix for wireless electric vehicle charging,” *IEEE Sensors J.*, vol. 19, no. 5, pp. 1683–1692, Mar. 2019.

[24] B. Zhang, Q. Chen, G. Ke, L. Xu, X. Ren, and Z. Zhang, “Coil positioning based on DC pre-excitation and magnetic sensing for wireless electric vehicle charging,” *IEEE Trans. Ind. Electron.*, vol. 68, no. 5, pp. 3820–3830, May 2021.

[25] Y. Gao, C. Duan, A. A. Oliveira, A. Ginart, K. B. Farley, and Z. T. H. Tse, “3-D coil positioning based on magnetic sensing for wireless EV charging,” *IEEE Trans. Transp. Electrific.*, vol. 3, no. 3, pp. 578–588, Sep. 2017.

[26] L. Tan *et al.*, “Mesh-based accurate positioning strategy of EV wireless charging coil with detection coils,” *IEEE Trans. Ind. Informat.*, vol. 17, no. 5, pp. 3176–3185, May 2021.

[27] S. Y. Jeong, H. G. Kwak, G. C. Jang, S. Y. Choi, and C. T. Rim, “Dual-purpose non-overlapping coil sets as metal object and vehicle position detections for wireless stationary EV chargers,” *IEEE Trans. Power Electron.*, vol. 33, no. 9, pp. 7387–7397, Sep. 2018.

[28] A. Babu and B. George, “Sensor system to aid the vehicle alignment for inductive EV chargers,” *IEEE Trans. Ind. Electron.*, vol. 66, no. 9, pp. 7338–7346, Sep. 2019.

[29] Z. Zhang, S. Zheng, D. Xu, P. T. Krein, and H. Ma, “An orthogonal decoupled transformer design for inductive power transfer applications,” in *Proc. IEEE Int. Symp. Ind. Electron.*, Jun. 2020, pp. 1587–1592.

[30] Z. Zhang, S. Zheng, Z. Yao, D. Xu, P. T. Krein, and H. Ma, “Analysis, design, and implementation of a spatially nested magnetic integration method for inductive power transfer systems,” *IEEE Trans. Power Electron.*, vol. 36, no. 7, pp. 7537–7549, Jul. 2021.

[31] R. L. Steigerwald, “A comparison of half-bridge resonant converter topologies,” *IEEE Trans. Power Electron.*, vol. 3, no. 2, pp. 174–182, Apr. 1988.

[32] Z. Pantic, S. Bai, and S. M. Lukic, “ZCS *LCC*-compensated resonant inverter for inductive-power-transfer application,” *IEEE Trans. Ind. Electron.*, vol. 58, no. 8, pp. 3500–3510, Aug. 2011.

[33] S. Li, W. Li, J. Deng, T. D. Nguyen, and C. C. Mi, “A double-sided LCC compensation network and its tuning method for wireless power transfer,” *IEEE Trans. Veh. Technol.*, vol. 64, no. 6, pp. 2261–2273, Jun. 2015.

[34] S. Y. Jeong, J. H. Park, G. P. Hong, and C. T. Rim, “Autotuning control system by variation of self-inductance for dynamic wireless EV charging with small air gap,” *IEEE Trans. Power Electron.*, vol. 34, no. 6, pp. 5165–5174, Jun. 2019.

[35] H. Hao, G. A. Covic, and J. T. Boys, “A parallel topology for inductive power transfer power supplies,” *IEEE Trans. Power Electron.*, vol. 29, no. 3, pp. 1140–1151, Mar. 2014.

[36] Q. Deng, P. Sun, W. Hu, D. Czarkowski, M. K. Kazimierczuk, and H. Zhou, “Modular parallel multi-inverter system for high-power inductive power transfer,” *IEEE Trans. Power Electron.*, vol. 34, no. 10, pp. 9422–9434, Oct. 2019.

[37] H. Zhou *et al.*, “Input-series output-equivalent-parallel multi-inverter system for high-voltage and high-power wireless power transfer,” *IEEE Trans. Power Electron.*, vol. 36, no. 1, pp. 228–238, Jan. 2021.

[38] X. Mou, O. Groling, A. Gallant, and H. Sun, “Energy efficient and adaptive design for wireless power transfer in electric vehicles,” *IEEE Trans. Ind. Electron.*, vol. 64, no. 9, pp. 7250–7260, Sep. 2017.

Zhuhaobo Zhang (Student Member, IEEE) received the B.S. degree in electrical engineering in 2017 from Zhejiang University, Hangzhou, China, where he is currently working toward the Ph.D. degree in electrical engineering.

His main research interests include wireless power transfer, resonant converters, and electric vehicle charging systems.

Shaoting Zheng (Student Member, IEEE) received the B.S. degree in electrical engineering in 2019 from Zhejiang University, Hangzhou, China, where he is currently working toward the Ph.D. degree in electrical engineering.

His research interests include wireless power transfer.

Zirui Yao (Student Member, IEEE) received the B.S. degree in electrical engineering in 2018 from the South China University of Technology, Guangzhou, China, where he is currently working toward the Ph.D. degree in electrical engineering.

His research interests include inductive power transfer and resonant converters.

Dehong Xu (Fellow, IEEE) received the B.S., M.S., and Ph.D. degrees from the College of Electrical Engineering, Zhejiang University, Hangzhou, China, in 1983, 1986, and 1989, respectively.

Since 1996, he has been a Full Professor with the College of Electrical Engineering, Zhejiang University. From June 1995 to May 1996, he was a Visiting Scholar with the University of Tokyo, Tokyo, Japan. From June 2000 to December 2000, he was a Visiting Professor with the Center for Power Electronics Systems, Virginia Tech, Blacksburg, VA, USA. From February 2006 to April 2006, he was a Visiting Professor with ETH, Switzerland. His current research interests include power electronics topologies and control and power conversion for renewable energy and energy saving. He has authored or coauthored 8 books and more than 270 IEEE journal and conference papers. He holds more than 50 patents.

Dr. Xu was an IEEE PELS Distinguish Lecturer from 2015 to 2018. He was the recipient of seven IEEE journal and conference paper awards. He was also the recipient of the IEEE PELS R. D. Middlebrook Achievement Award in 2016.

Philip T. Krein (Life Fellow, IEEE) received the B.S. degree in electrical engineering and the A.B. degree in economics and business in 1978 from Lafayette College, Easton, PA, USA, and the M.S. and Ph.D. degrees in electrical engineering from the University of Illinois at Urbana-Champaign, Champaign, IL, USA, in 1980 and 1982, respectively.

He was an Engineer with Tektronix, Beaverton, OR, USA, and then returned to the University of Illinois at Urbana-Champaign. From 1997 to 1998, he was a Senior Fulbright Scholar with the University of Surrey, Guildford, U.K. From 2003 to 2014, he was the founder and Director of SolarBridge Technologies, Inc., Austin, TX, USA, a developer of ac photovoltaic panels. From 2016 to 2020, he was the Executive Dean of the Zhejiang University/University of Illinois at Urbana-Champaign Institute, Haining, China. He holds the Grainger Endowed Chair Emeritus in Electric Machinery and Electromechanics with the University of Illinois at Urbana-Champaign and is an Adjunct Distinguished Professor with Zhejiang University. He holds 42 U.S. patents. His current research interests include all aspects of power electronics, machines, drives, and electric transportation, with emphasis on nonlinear control approaches.

Dr. Krein is a past President of the IEEE Power Electronics Society, a past member of the IEEE Board of Directors, a past Chair of the IEEE Transportation Electrification Community, and an Associate Editor for the IEEE OPEN JOURNAL OF POWER ELECTRONICS. He is a Registered Professional Engineer in Illinois and Oregon. He is a Fellow of the U.S. National Academy of Inventors and a member of the U.S. National Academy of Engineering. He was the recipient of the IEEE William E. Newell Power Electronics Award in 2003 and the IEEE Transportation Technologies Award in 2021.

Hao Ma (Senior Member, IEEE) received the B.S., M.S., and Ph.D. degrees in electrical engineering from Zhejiang University, Hangzhou, China, in 1991, 1994, and 1997, respectively.

Since 1997, he has been a Lecturer, Associate Professor, and Professor with Zhejiang University. From September 2007 to September 2008, he was a Delta Visiting Scholar with the North Carolina State University. He is the Vice Dean of the ZJU-UIUC Institute. He has authored 2 books and authored or coauthored more than 200 technical papers. His research interests include advanced control in power electronics, wireless power transfer, fault diagnosis of power electronic circuits and systems, and application of power electronics.

Dr. Ma is currently the Vice-President of China Power Supply Society. He was the AdCom member of the IEEE Industrial Electronics Society, the Technical Program Chair of the IEEE ISIE 2012, IEEE PEAC 2014, IEEE PEAC 2018, and IEEE PEAS 2021.